ORIGINAL RESEARCH

Removal of Neutral Red Dye via Electro-Fenton Process: A Response Surface Methodology Modeling

Masoud Ebratkhahan[1] · Samin Naghash Hamed[1] · Mahmoud Zarei[1] · Abbas Jafarizad[2] ·
Mohammad Rostamizadeh[3]

Abstract

Recycling wastewater for industries and providing future security for humans and the environment are important issues that need to be concerned. In this study, electro-Fenton (EF) process using graphite electrodes as cathode and anode and its application in removing neutral red (NR) dye using response surface methodology (RSM) was examined. Ultraviolet–visible spectroscopy (UV–Vis), Fourier-transform infrared spectroscopy (FT-IR), X-ray diffraction (XRD), Brunauer–Emmett–Teller (BET), temperature programmed desorption (TPD), total organic carbon (TOC), and gas chromatography–mass spectrometry (GC-MS) analysis were performed to analyze the degradation of the NR and characterization of the nanocatalysts. The effects of operational parameters such as applied current, amount of catalyst, initial NR concentration, reaction time, and pH on the decolorization efficiency of the NR were examined. The results showed that in the applied current of 200 mA, the amount of Fe^{2+} 2%, the initial NR concentration of 40 mg/L, and pH = 3 during 40 min of reaction time, the maximum decolorization efficiency value was 85.88% at homogenous EF, and 90.32% and 92.44% at heterogeneous EF using HZC and FeZC nanocatalysts, respectively. The results of the experimental part were compared by predictions via Minitab 16 software. The correlation coefficient found between the experimental and the model results was 99.7%.

Keywords Advanced oxidation process · Electro-Fenton · Hydroxyl radical · Neutral red · Response surface methodology

✉ Mahmoud Zarei
  mzarei@tabrizu.ac.ir; zarei90211@yahoo.com

  Masoud Ebratkhahan
  masoudebratkhahan@yahoo.com

  Samin Naghash Hamed
  samin.hamed1997@gmail.com

  Abbas Jafarizad
  Jafarizad.abbas@gmail.com

  Mohammad Rostamizadeh
  Rostamizadeh@sut.ac.ir

[1] Research Laboratory of Environmental Remediation, Department of Applied Chemistry, University of Tabriz, 51666-16471 Tabriz, Iran

[2] Department of Chemical Engineering, School of Chemistry, Sahand University of Technology, Tabriz, Iran

[3] Department of Chemical Engineering, School of Environment, Sahand University of Technology, Tabriz, Iran

Introduction

During recent decades, advanced oxidation processes (AOPs) have proven a promising effect at organic pollutant degradation from wastewaters. The basis of AOPs is the in situ production of free hydroxyl radical ($^\bullet$OH) in aqueous solution via chemical, photochemical, electrochemical, or photocatalytic methods [1, 2]. Hydroxyl is a strong oxidant that is able to mineralize most of the organic pollutants unselectively through hydrogen abstraction, electron transfer reaction, and electrophilic addition on double bond, finally converting them into CO_2, H_2O, and inorganic ions [3, 4]. The AOP method consists of different methods including ozonation [5], UV irradiation [6], ultrasonication [7], Fenton [8], and electro-Fenton (EF) [9].

Fenton reaction, which is the aqueous combination of Fe^{2+} and H_2O_2, is considered a promising environmental remediation technology. This method is simple, does not need any special equipment, highly efficient in organic pollutant removal, and is an environmentally safe method. Although this method has high efficiency at the oxidation of organic pollutants, the application of this method at a large scale has been restricted due to the shipment and storage problems of H_2O_2 and the generation of

iron sludge. Newly, to overcome the mentioned problems, the EF process has been developed. This process includes the ferrous ion addition and in situ electro-generation of H_2O_2 [10–12]. H_2O_2 can be produced by a two-electron reduction of oxygen at the appropriate cathodic potential on specific electrodes such as graphite [13], activated carbon fiber [14], carbon felt [15], graphene [16], C60-carbon nanotube composite [17], and gas diffusion electrode [18–20]. The reactions occurred can be expressed as follows (Eq. 1 and 2):

$$O_2 + 2H^+ + 2e^- \rightarrow H_2O_2 \qquad (1)$$

$$Fe^{2+} + H_2O_2 \rightarrow Fe^{3+} + \,^\bullet OH + OH^- \qquad (2)$$
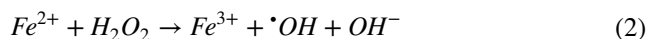
The advantages of the EF process include the following: (1) continuous in situ generation of H_2O_2 (Eq. 1), which eliminates shipment and storage costs of H_2O_2; (2) the reaction occurs easily at ambient temperature and pressure; (3) Fe^{2+} can be electrochemically regenerated at the cathode; therefore, the amount of iron sludge will be reduced (Eq. 3); and (4) air or oxygen flow enhances the mixing rate of EF reaction [21–25].

$$Fe^{3+} + e^- \rightarrow Fe^{2+} \qquad (3)$$

The concentration of H_2O_2 is an essential factor in the efficiency of pollutant degradation in the Fenton reaction. Hence, an efficient cathode system for significant production of H_2O_2 and pollutant degradation seems to be necessary [25–27].

The elimination of dyes from wastewater is one of primary environmental concerns. More than 10,000 dyes are probably consumed in different industries such as textiles, leather, rubber, plastics, paper, food, cosmetics, and mineral processing industries. The concentration of these pollutants varies at 10–10.000 mg/L range [28, 29]. Synthetic dyes represent a massive problem due to their resistivity in biological treatment. Dye is one of the most obnoxious pollutants due to the following: (1) it is observable and even small quantities (≥ 0.005 mg/L) are not allowed [30], (2) the color of the dye can interfere sunlight transmission into natural streams, and (3) many of dyes and their intermediate products are toxic to aquatic life, carcinogenic and mutagenic to humans [31].

Neutral red (NR) is a cationic dye. It is widely applied as a pH indicator in laboratories and for nuclear counterstaining in biological research. This dye is considered toxic and hazardous because when it is decomposed, it gives out hazardous products, such as carbon monoxide, nitrogen oxides, and hydrogen chloride. These products may cause serious health problems for humans and animals. Therefore, NR draws significant attention to the innovation of effective techniques for its removal [32].

In this study, the removal of NR from the aqueous environment by the EF process using a couple of graphite electrodes as cathode and anode and its effective parameters effect were investigated. To find optimum amounts of variables, response surface methodology (RSM) was applied via Minitab 16 software. Finally, a verification study of the analysis including ultraviolet–visible spectroscopy (UV–Vis), Fourier-transform infrared spectroscopy (FT-IR), X-ray diffraction (XRD), Brunauer–Emmett–Teller (BET), temperature programmed desorption (TPD), total organic carbon (TOC), and gas chromatography–mass spectrometry (GC-MS) was performed using the optimum operational conditions.

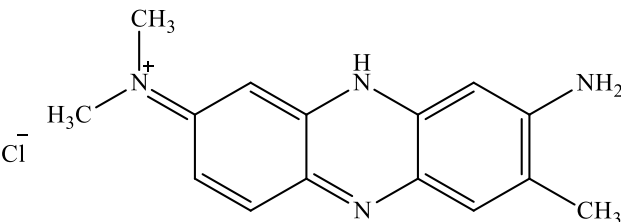## Materials and Methods

Chemicals

Sodium aluminate ($NaAlO_2$, Al_2O_3, 55 wt%), silicic acid ($SiO_2 \cdot xH_2O$, > 99 wt%), iron nitrate ($Fe(NO_3)_2 \cdot 9H_2O$), tetrapropyl ammonium bromide (TPABr, $C_{12}H_{28}BrN$), ammonium nitrate (NH_4NO_3), sodium sulfate (Na_2SO_4), sulfuric acid (H_2SO_4), and sodium hydroxide (NaOH) purchased from Merck (Germany).

NR, cationic dye, was selected as the model pollutant and purchased from Boyakhsaz Co. (Iran). The chemical properties of the NR are presented in Table 1.

Instruments and Characterizations

For measuring the pH of the solution, pH-meter (AZ 86502, Iran) was used. The stirring of samples was performed via a magnetic stirrer (Philler scientific, Iran). To generate the

Table 1 Characteristics of NR

Structure	λ_{max} (nm)	Formula	M_w (g/mol)
	519	$C_{15}H_{17}ClN_4$	288.78

electricity current of the process, ADAK-PS405 power supply was applied. The decolorization of the NR was monitored by SPECORD 250 UV–Vis spectrophotometer (Analytik Jena, Germany). The absorbance of NR was studied at 519 nm.

For FT-IR measurements, Nexus Model Infrared Spectrophotometer (Nicolet Co, USA) was applied at 4 cm^{-1} resolution. XRD experimentations were performed by a D8 Advance Bruker AXS X-ray diffractometer with Ni-filtered Cu Kα radiation ($\lambda = 0.15418$ nm) at 2θ range of 4–50° at 40 kV.

To investigate the surface area of nanocatalysts, BET measurements were done. For this purpose, the degassing of powders was performed for 3 h at 300 °C. Then, the total surface area (S_{BET}), total volume (V_{total}), micropore volume (V_{micro}), and mesopore volume (V_{meso}) of nanocatalysts were calculated. For calculating the mentioned parameters, the BET isothermal equation, nitrogen adsorbed volume at $P/P_0 = 0.99$,

Table 2 Coded levels and the natural values of the independent test variables

Variables	Ranges and levels				
	−2	−1	0	+1	+2
pH (X_1)	2	4	6	8	10
Applied current (mA) (X_2)	100	200	300	400	500
Time (min) (X_3)	20	40	60	80	100
Fe ion (%) (X_4)	1	2	3	4	5
[NR]$_0$ (mg/L) (X_5)	10	20	30	40	50

t-plot method, and the difference of the total calculated data and the corresponding micropore data were applied.

Temperature programmed desorption of ammonia (NH$_3$-TPD, Micromeritics, USA) with an on-line TCD detector

Table 3 The 5-factor central composite design matrix and the value of response function (decolorization efficiency %)

Run	pH	Current (mA)	Time (min)	Fe ion (%)	[NR] (ppm)	Decolorization efficiency (DE %)	
						Experimental	Predicted
1	4	300	60	3	30	82.15	81.7172
2	5	400	40	2	40	61.11	61.6005
3	5	400	80	2	20	54.11	54.7272
4	4	300	60	5	30	57.02	57.1110
5	4	300	60	3	30	80.87	81.7172
6	5	200	40	4	40	65.87	65.7614
7	2	300	60	3	30	84.71	84.7927
8	5	400	40	4	20	60.49	61.0755
9	4	300	60	3	30	80.73	81.7172
10	3	200	80	2	20	80.35	80.3722
11	4	300	20	3	30	75.57	74.9194
12	4	300	60	3	10	74.02	73.1160
13	5	200	40	2	20	69.09	69.4789
14	5	200	80	4	20	76.60	76.6180
15	4	300	60	3	30	81.86	81.7172
16	3	400	40	4	40	84.98	85.0722
17	4	300	60	1	30	61.13	60.4160
18	4	100	60	3	30	84.70	85.1844
19	4	500	60	3	30	67.34	66.2327
20	3	400	80	2	40	82.03	82.1539
21	5	200	80	2	40	74.68	74.6030
22	4	300	60	3	30	81.30	81.7172
23	3	200	80	4	40	74.32	73.8447
24	6	300	60	3	30	65.21	64.5044
25	4	300	60	3	50	85.02	85.3010
26	4	300	60	3	30	82.77	81.7172
27	3	200	40	2	40	85.88	85.7755
28	3	200	40	4	20	74.13	74.1205
29	3	400	80	4	20	61.12	61.3389
30	4	300	100	3	30	74.50	74.5277
31	3	400	40	2	20	59.98	60.5697
32	5	400	80	4	40	58.11	58.2297

was applied for studying the acidity of the samples. The textural properties of the samples were identified via N_2 adsorption–desorption technique at -196.2 °C (Quantachrome, USA).

For TOC measurements, a TOC analyzer (Shimadzu, Japan) was applied. An Agilent 6890 gas chromatography coupled with an Agilent 5973 mass spectrometer (Agilent Technologies, Palo Alto, CA) was used for GC-MS analysis. The temperature programming of this analysis was done according to our previous work [13].

Experimental Design

In this research, the central composite design (CCD) with five levels was applied to optimize the EF method. For investigating the influence of the operational parameters on the NR degradation efficiency, five factors, including pH (X_1), applied current (X_2), reaction time (X_3), amount of catalyst (X_4), and initial NR concentration (X_5), were chosen. Thirty-one experiments were recommended by the software. The range of parameters and applied levels are presented in Table 2.

Electrochemical System

EF treatments were performed in a 100-mL glass beaker considered as undivided cell at room temperature under a magnetic stirrer using a couple of graphite sheets with dimensions of 1 cm × 3 cm × 0.3 cm as electrodes. For NR solution preparation, 50 mL of NR dye solution, iron(II) sulfate solution (0.1 M) and 5 mL of sodium sulfate solution (0.05 M) were added, respectively. The pH was adjusted via adding H_2SO_4 and NaOH to the solution. Then, the needed oxygen was provided via air injector to produce the required H_2O_2. The electrical current of the process was conducted with a power supply at the range of 0.1–0.5 A. For the heterogeneous EF method, the provided catalysts were used instead of iron(II) sulfate solution and the other chemicals were the same. The decolorization efficiency of NR was measured by Eq. 4, which A_0 and A_t are the absorbance of initial NR solution and the absorbance NR after t minutes of reaction, respectively.

$$\text{Decolorization efficiency}(\%) = \frac{A_0 - A_t}{A_0} \times 100 \quad (4)$$

Catalyst Synthesis

The zeolite nanocatalysts were prepared by the hydrothermal method and impregnation with the iron promoter (1 wt%) at one of the samples according to Rostamizadeh et al. [33]. In the current study, the crystallization of the nanocatalyst was performed for 48 h at a temperature of 180°C under autogenous pressure in an autoclave. The obtained powder was washed several times. Then, it was dried for 48 h at 105°C. Then, the calcination of the nanocatalyst was performed for 12 h at a temperature of 530°C. The heating rate of the furnace was 3°C/min with air flow. The powder was ion-exchanged four times by 1 M solution of NH_4NO_3 at 90°C for 10 h, following with drying at 105°C overnight and calcination at 540°C in air for 12 h (3°C/min). The parent nanocatalyst was denoted as HZC zeolite. The iron promoter was incorporated on the parent HZC through a multi-step impregnation in rotary evaporator including the following temperatures and pressures: (1) 65°C and 300 mmHg for 60 min, (2) 70°C and 250 mmHg for 30 min, (3) 70°C and 200 mmHg for 30 min, (4) 75°C and 200 mmHg for 30 min. Finally, the solution was dried at 110°C for 12 h to obtain Fe impregnated ZSM-5 nanocatalyst (FeZC).
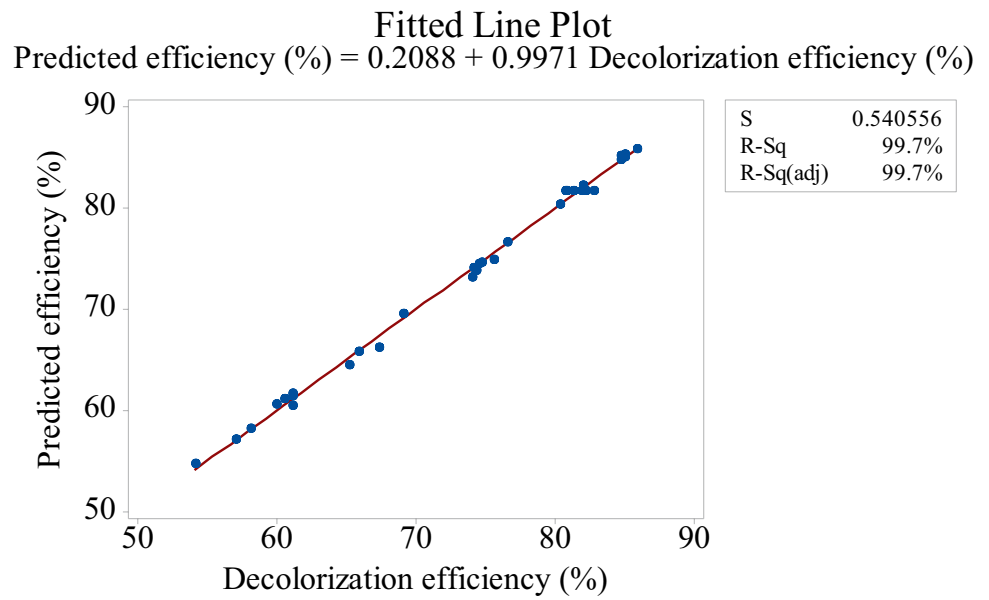
Results and Discussions

EF Process Optimizing with RSM

For this part of the research, Minitab 16 software was applied and 31 tests were designed by the software. Experiments were performed according to Table 3. According to the experimental results, the coefficients of correlation and relationship was obtained between the response variable and independent variables according to Eq. 5:

$$\begin{aligned} Y = &-53.74 + 18.09X_1 + 0.0055X_2 + 0.9978X_3 + 35.87X_4 + 1.918X_5 \\ &- 0.01616X_1X_2 + 0.0440X_1X_3 + 0.986X_1X_4 - 0.3259X_1X_5 \\ &- 0.000693X_2X_3 + 0.01659X_2X_4 + 0.003122X_2X_5 - 0.0951X_3X_4 \\ &- 0.00537X_3X_5 - 0.1827X_4X_5 - 1.767X_1^2 - 0.000150X_2^2 \\ &- 0.004371X_3^2 - 5.738X_4^2 - 0.00627X_5^2 \end{aligned}$$

$$(5)$$

In this equation, Y is the response variable (decolorization efficiency) and X_i is the experimental levels of the variables. Table 3 shows the experimental and predicted results by

Table 4 Analysis of variance (ANOVA) for fit of decolorization efficiency from central composite design

Source variations	Sum of squares	Degree of freedom	Adjusted of mean square	F value	P value
Regression	26	3078.45	118.402	189.88	0.000
Errors	5	3.12	0.624		
Total	31	3081.56			

$R^2 = 99.7\%$, Adj-$R^2 = 99.37\%$

Fig. 1 Comparison of experimental and predicted decolorization efficiency results

Fitted Line Plot
Predicted efficiency (%) = 0.2088 + 0.9971 Decolorization efficiency (%)

| S | 0.540556 |
| R-Sq | 99.7% |
| R-Sq(adj) | 99.7% |

the software based on the Eq. 5 in uncoded form. Based on the results, it can be concluded that the resulted model can accurately modeling the experimental results and can be used to predict the output variable under other conditions.

Analysis of variance (ANOVA) is commonly used to test the significance and suitability of the model. Table 4 shows

the ANOVA results. The obtained correlation coefficient ($R^2 = 0.997$) is acceptable (Fig. 1), indicating how much variability in the response variable can be explained by the experimental factors and their interactions. The obtained value indicates that approximately 99.7% of the variability in decolorization efficiency can be justified by the independent

Fig. 2 Pareto graphic analysis of parameters
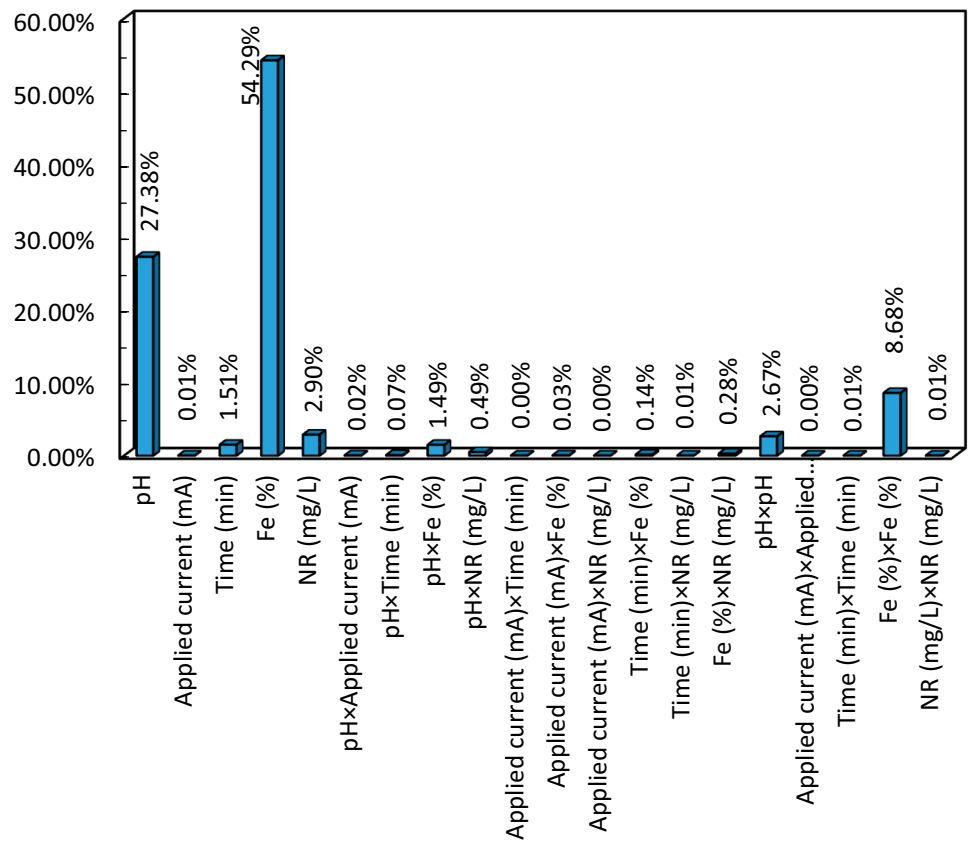
variables and the model is unable to explain only 0.3% of the variation.

The variables and their interactions impact on the response value can be calculated via Pareto analysis. Each parameter's influence is determined via Eq. 6 and the obtained coefficients of each parameter via Eq. 5.

$$P_i = \left(\frac{a_i^2}{\sum a_i^2} \right) \times 100 \, i \neq 0 \tag{6}$$

In this equation, P_i represents the effect of each parameter and the a_i is related to each parameter's coefficient. Figure 2 shows each parameter's impact and their interactions according to Pareto analysis. According to the results, Fe (%) amount and pH have the most influence among parameters, respectively.

The obtained F value of the model (the ratio of the mean squares to the regression or model and the residuals) is greater than the critical value, indicating that the factors adequately represent the data changes from their mean value
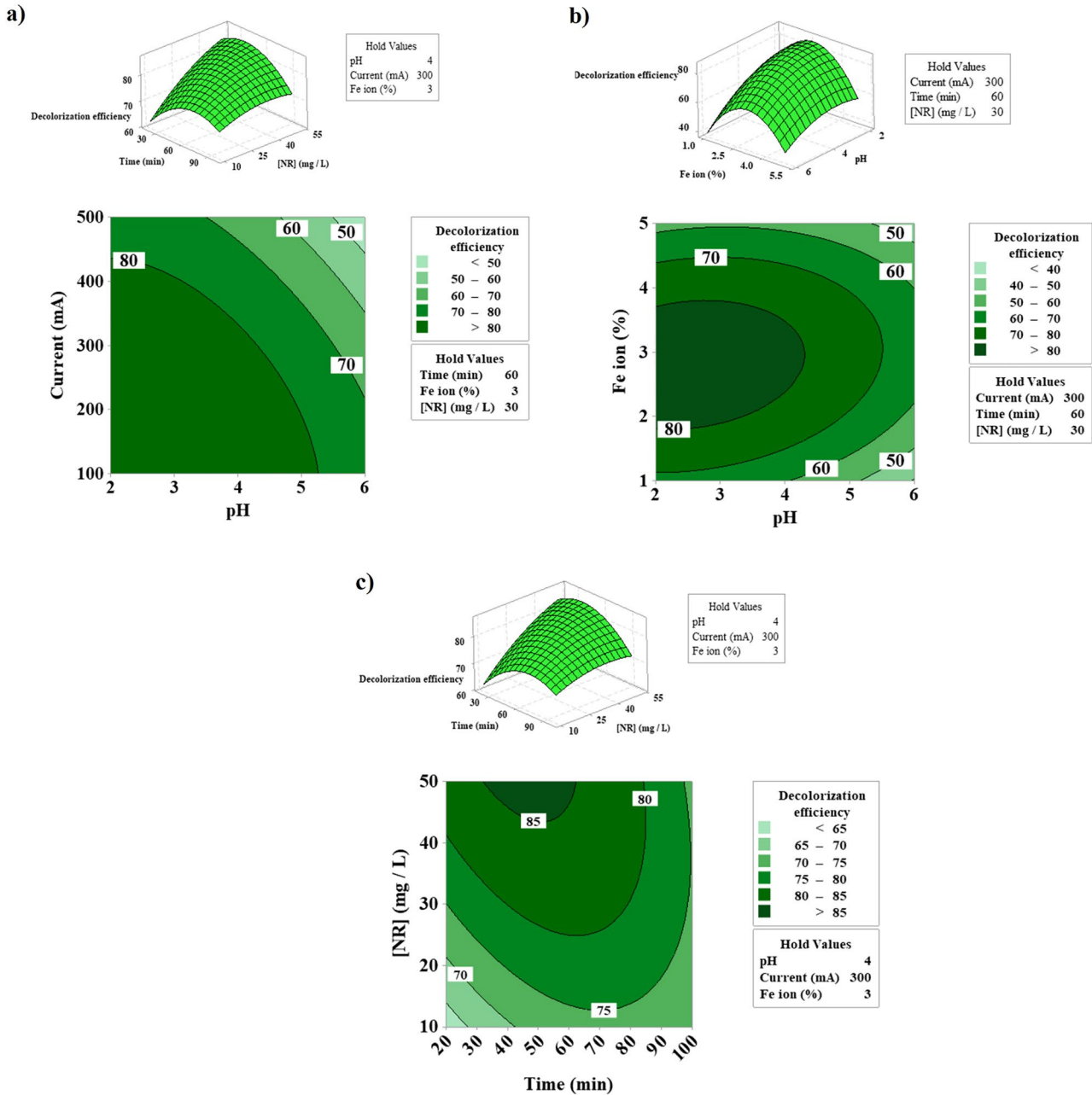
Fig. 3 The response surface plots and contour plots of the decolorization efficiency (DE. %) as the function of **a)** applied current (mA) and pH, **b)** pH and Fe ion amount (%), and **c)** initial NR concentration (mol/L) and EF time (min)

and the effects of the factors estimated in the model are true and accurate [34, 35]. If the obtained F value is compared with the critical F values reported in the statistical tables at degrees 30 and 32, it can be seen that the obtained F in this experiment is greater than the critical F value and the null hypothesis is rejected, which means the origin of the regression or model changes and the residuals are not the same [36].

Effects of Operational Parameters on the Decolorization Efficiency of NR

Influence of Applied Current and pH on Decolorization Efficiency

Figure 3a shows two-dimensional and three-dimensional graphs of the decolorization efficiency as a function of applied current and pH for a solution with an initial NR concentration of 30 mg/L, reaction time of 60 min and Fe ion amount of 3% (V/V). According to this, at pH = 3, by increasing the current intensity about 300 mA, the decolorization efficiency is slightly increased and after 400 mA, it is rapidly decreased.

Increasing the current intensity to the optimum amount leads to the formation of more H_2O_2 in the cathode, and thus the production of $^\bullet OH$. It also increases the hydrolysis of the water molecules and accelerates the EF process by accelerating electrical coagulation. On the other hand, increasing the current intensity above the optimum value results in competitive electrode reactions such as oxygen depletion at the anode and hydrogen formation at the cathode, which results in a decrease in the $^\bullet OH$ concentration in the solution and decreases the decolorization efficiency [37, 38].

pH is one of the most critical parameters in the EF process. It directly affects the oxidation of organic compounds and $^\bullet OH$ production [39]. Studies in this field show that the effect of the initial pH of the environment varies greatly depending on the type of contaminant in the different processes.

Table 5 Optimum operating parameters for maximum removal efficiency

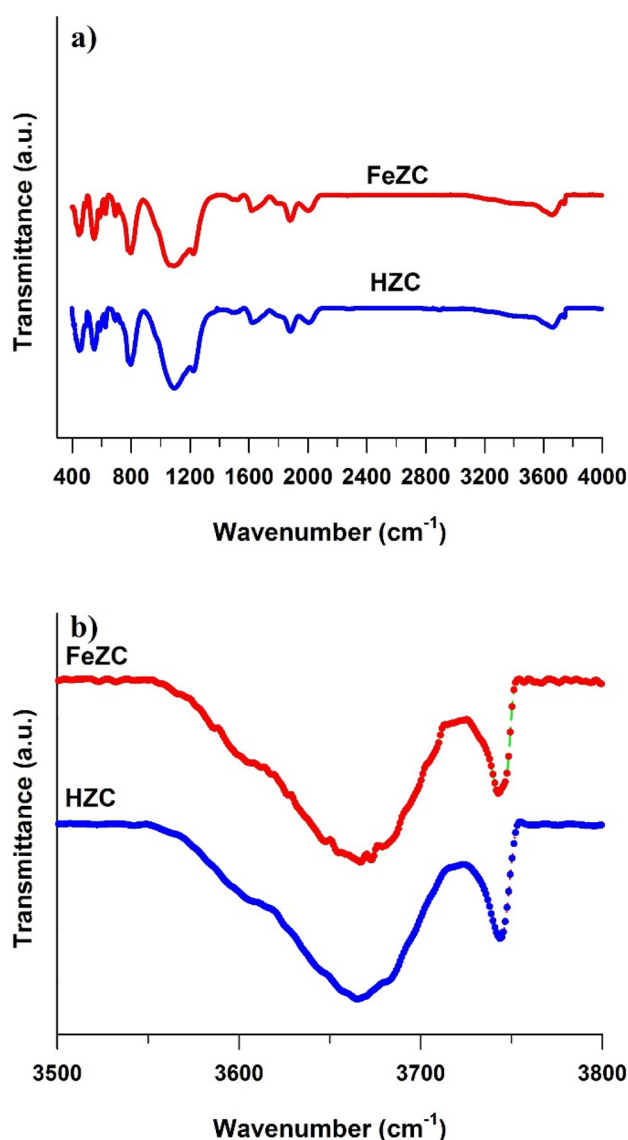| Variable	Optimum value
pH (X_1)	3
Applied current (mA) (X_2)	200
Time (min) (X_3)	40
Fe ion (%) (X_4)	2
$[NR]_0$ (mg/L) (X_5)	40
Predicted degradation efficiency (%)	85.77
Experimental degradation efficiency (%)	85.88

Fig. 4 FTIR spectra of nanocatalysts in the range of **a)** 400–4000 cm^{-1} and **b)** 3500–3800 cm^{-1}

At very low pH, available or electronically produced H_2O_2 cannot be decomposed by the Fe^{2+} ions present in the reaction medium to $^\bullet OH$. Therefore, it absorbs a positive charge (proton) and converts it to an oxonium ion (Eq. 7), which is more stable than H_2O_2 and reducing its reaction with Fe^{2+}, resulting in a decrease in $^\bullet OH$ production and process efficiency [40].

$$H_2O_2 + 4H^+ \rightarrow 2H_3O^{2+} \tag{7}$$

At high pH, H_2O_2 is unstable and may decompose spontaneously according to Eq. 8.

$$H_2O_2 \rightarrow O_2 + H_2 \tag{8}$$

In this range, Fe^{2+} and Fe^{3+} are converted to $Fe(OH)_2$ and $Fe(OH)_3$ through the reaction with ^-OH, respectively. $Fe(OH)_3$ exits the EF process cycle after formation but can promote electrical coagulation, while $Fe(OH)_2$ may lead to the development of the EF process (Eq. 9) [37].

$$2H_2O_2 + Fe(OH)_2 \rightarrow Fe_2O_3 + H_2O + 2HO \qquad (9)$$
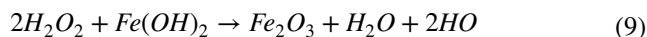
Influence of pH and Fe Ion Amount on Decolorization Efficiency

In Fig. 3b, the simultaneous effect of initial solution pH and Fe ion amount on the decolorization efficiency was investigated at initial NR concentration of 30 mg/L, applied current of 300 mA and 60 min of reaction time. These two-dimensional and three-dimensional curves show that by increasing until pH = 3, the decolorization efficiency increases, and after this point, it decreases. Fe^{2+} amount also plays an important role in the NR removal during the EF process. It was observed by increasing the Fe^{2+} amount until 3% the decolorization efficiency increases. By adding more amount of Fe ion and passing the optimum amount, the decolorization efficiency decreases.

Influence Initial NR Concentration and Reaction Time on Decolorization Efficiency

Figure 3c shows two-dimensional and three-dimensional graphs of decolorization efficiency as a function of initial NR concentration and reaction time. It can be seen by increasing the initial NR concentration to the optimum level; the decolorization efficiency gradually increases, whereas, at the same conditions with lower initial concentration, the decolorization efficiency quickly reaches higher efficiencies. It must be noted after passing the optimum initial NR concentration, the amount of hydroxyl radical will not be sufficient to remove the high contaminant concentration and the decolorization efficiency will be decreased [41]. At higher initial NR concentrations, the optimal time range for NR decolorization is more narrow than it is at lower concentrations.
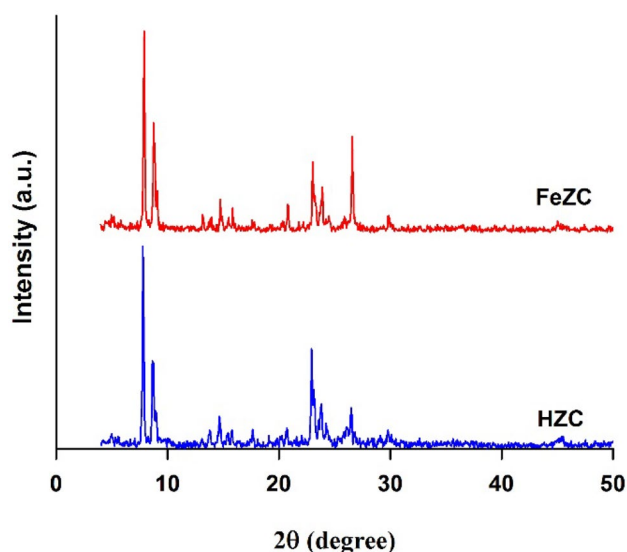

Fig. 5 The XRD patterns of nanocatalysts

Determination of Optimum Conditions for NR Decolorization

The optimal way to remove NR is to reach maximum efficiency. Therefore, using the Minitab 16 software, optimal test conditions were determined as stated in Table 5. The results showed a maximum of 85.88% NR removal at the applied current of 200 mA, the amount of Fe^{2+} 2%, the initial NR concentration of 40 mg/L, and pH = 3 during 40 min of reaction time. After obtaining the optimum conditions, an experiment was performed at optimal conditions and the results showed that there is a fairly good agreement between the experimental value (85.88%) and the value predicted by the model (85.77%). This demonstrates the success of using the RSM in modeling and optimizing the homogeneous EF process.

Nanocatalyst Characterization

FT-IR spectra of the synthesized nanocatalysts were documented in the range of 400–4000 cm^{-1}. The bands nearby 450 cm^{-1} assigned to the internal SiO_4 and AlO_4 tetrahedral. The band about the wavelength of 550 cm^{-1}

Table 6 Relative crystallinity and textural data of the nanocatalysts

Sample	Crystallinity (%)	S_{BET} (m^2 g^{-1})	V_{total} (cm^3 g^{-1})	V_{micro} (cm^3 g^{-1})	V_{meso} (cm^3 g^{-1})
HZC	100.00	321.10	0.19	0.13	0.06
FeZC	72.41	294.40	0.17	0.11	0.06

Table 7 Acidity and strong/weak ratio

Sample	Acidity (mmol NH$_3$ g^{-1})			Strong/weak
	Weak	Strong	Total	
HZC	0.53	0.53	1.06	1.00
FeZC	0.43	0.53	0.96	1.23

Fig. 6 **a)** N_2 adsorption–desorption isotherm and **b)** pore size distribution of nanocatalysts
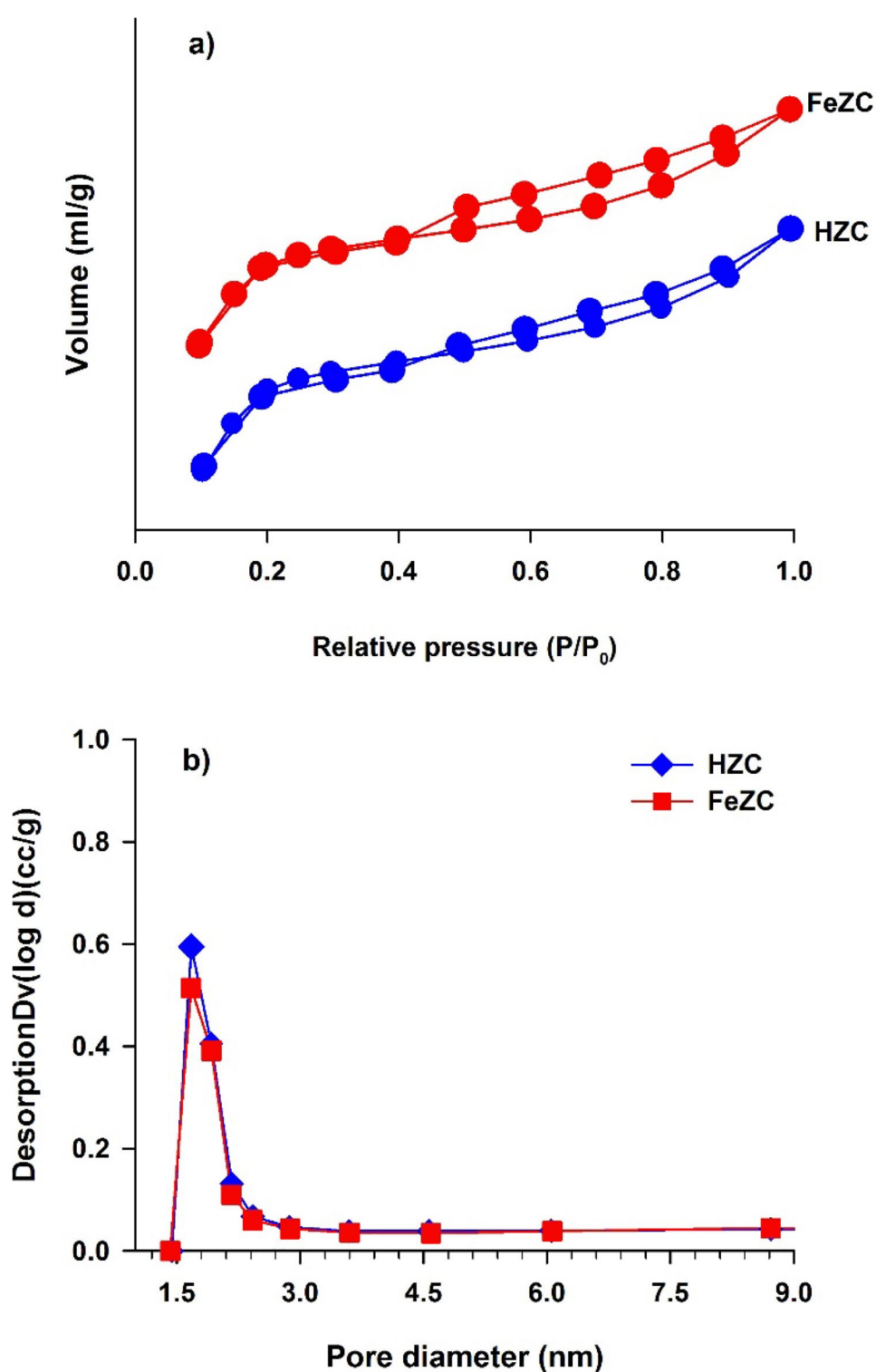
attributed to the zeolite with five-membered rings at HZC and FeZC (Fig. 4a). Surface hydroxyl groups band observed in the 3500–3800 cm^{-1} range (Fig. 4b). Recognized FT-IR bands for the vibration of bridging Si–OH-Al were at 3610 cm^{-1} and 3680 cm^{-1} range

[42]. The band at 3680 cm^{-1} belongs to extra-framework aluminum species (Al–OH) of the nanocatalysts [43, 44].

Figure 5 shows the XRD patterns of the synthesized HZC and FeZC nanocatalysts. The lower peak intensity of HZC comparing to FeZC at 2θ of 20–30° claims

Table 8 Identified by-products during electrolysis of NR
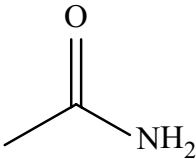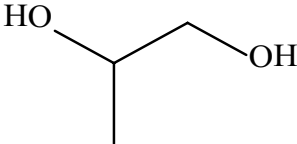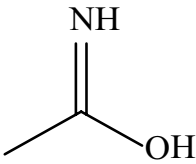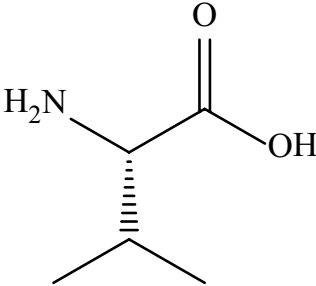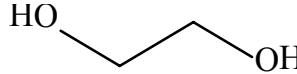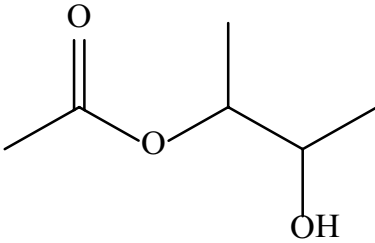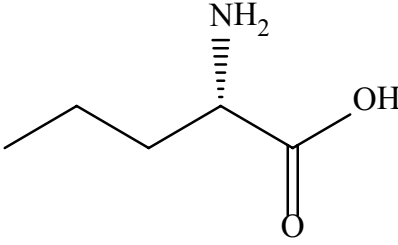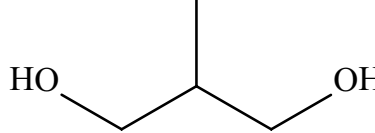
No	Compound name	Structure	Retention time (min)	Main fragments (m/z)
1	acetamide		1.917	77, 120, 144, 170
2	propane-1,2-diol		2.695	45, 73, 117, 147
3	ethanimidic acid		6.921	45, 75, 116, 147
4	(S)-2-amino-3-methylbutanoic acid		7.608	73, 144, 218
5	ethane-1,2-diol		7.867	45, 73, 103, 147, 191
6	2,3-butanediol monoacetate		8.081	43, 73, 117
7	(S)-2-aminopentanoic acid		8.111	45, 73, 144, 218
8	2-methyl-1,3-propanediol		8.538	73, 117, 147

Table 8 (continued)
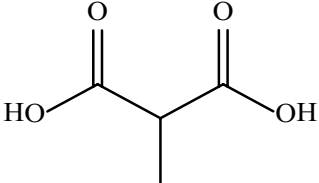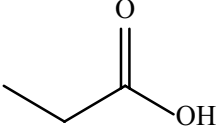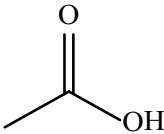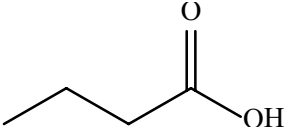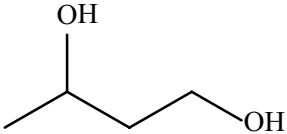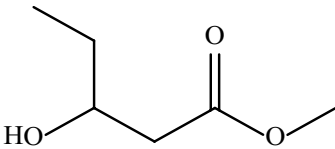
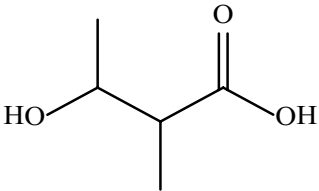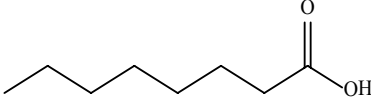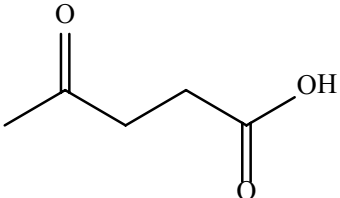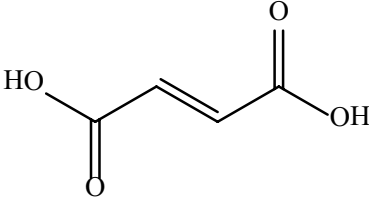| No	Compound name	Structure	Retention time (min)	Main fragments (m/z)
9	2-methylmalonic acid		10.140	45, 73, 147, 218, 247
10	propanoic acid		10.446	45, 73, 117, 147, 191, 219
11	acetic acid		10.766	45, 73, 147, 177, 205
12	butanoic acid		10.903	45, 73, 117, 147, 191, 233
13	1,3-butanediol		11.041	45, 73, 117, 147, 191
14	methyl 3-hydroxypentanoate		11.941	73, 147, 205, 233
15	3-hydroxy-2-methylbutanoic acid		12.093	45, 73, 131, 205, 233
16	octanoic acid		14.535	73, 117, 145, 201
17	4-oxopentanoic acid		18.837	43, 75, 145, 173

Table 8 (continued)

No	Compound name	Structure	Retention time (min)	Main fragments (m/z)
18	2-butenedioic acid		13.963	45, 73, 115, 147, 245

All values are corresponding to the trimethylsilyl derivative

amorphous SiO_2 was not entirely formed and crystallized in the HZC structure. According to Table 6, the relative crystallinity of HZC and FeZC nanocatalysts were high. Minor defects at the catalyst framework, which led to the amorphous peak at 2θ of 25.5–27° were observed. The reason for this phenomenon was dealumination over the impregnation process at the nanocatalysts, which results in a shift in the peak positions and slight framework damage [45]. The crystallinity reduction of the impregnated nanocatalysts was in accordance with the impurity formation. The lack of further peaks, which are related to the promoter, established the uniform promoter dispersion.

It was observed N_2 adsorption–desorption of HZC and FeZC nanocatalysts was a mixture of types I and IV isotherm according to Fig. 6a. The rectangular hysteresis loops at $P/P_0 = 0.5$–0.95 indicated the HZC and FeZC nanocatalysts structure are mesoporous, resulting from the capillary condensation [46]. Also, the crystal agglomeration was created an interparticle space at the mesoporous structure of nanocatalysts. The microporous structures of the HZC and FeZC nanocatalysts were proved by their high adsorption amount at $P/P_0 = 0.1$ [47]. Also, by analyzing the pore size distribution of HZC and FeZC, the mesoporous structure of nanocatalysts was confirmed (Fig. 6b). The primary pore diameter of the nanocatalysts was 1.70 nm. The calculated data in Table 6 also exhibited the high surface area and formation of mesopore nanocatalysts. The results obtained for BET were in accordance with the XRD results. The FeZC nanocatalyst represented higher total pore volume owing to the formation of mesopores during the impregnation process.

The NH_3-TPD measurements exhibited almost the same patterns for the HZC and FeZC with different strength and quantity of the acid sites (Table 7, Fig. 7a and b). The strong and weak acid sites of the HZC and FeZC nanocatalysts were characterized via a couple of desorption peaks. The temperature ranges of these peaks were 130–280°C and 300–500°C, respectively. The acid sites concentration was estimated via catalysts peak area. The

HZC almost involved the same quantity of strong and weak acid sites (0.53 mmol NH_3/g). The impregnation decreased nanocatalyst acidity due to Fe species involvement through the zeolite structure. This can be described by blocking pores and neutralizing surface acid sites with promoters [48]. The smaller effective ionic radii of Fe ion (about 0.77 Å [49]) made it possible to enter inside the channels of ZSM-5 (diameter of 5.5 Å) and interacted with interior acid sites.

TOC and GC-Mass Analysis

TOC analysis was also performed for the optimal sample to measure the degradation efficiency of the method. The TOC amount of NR over time is given in Fig. 8. The TOC amount of NR decreased over 2 h of reaction time, which indicates that the results of decolorization and degradation efficiency of NR are in good agreement and the mineralization efficiency reached 85.98%. This shows that NR has been successfully mineralized. The difference between obtained NR decolorization efficiency (92.44%) and degradation efficiency (85.98%) for heterogeneous EF can be attributed to the decomposition of organic materials and the formation of stable short-chain organic intermediates [13, 17].

GC-MS analysis was performed after preparing the optimal sample. The mass spectra obtained from GC-MS analysis were matched with the spectral information of the MS library (Wiley 7n) and 18 compounds were successfully identified according to Table 8 including the following: (1) acetamide, (2) propane-1,2-diol (3) ethanimidic acid, (4) (S)-2-amino-3-methylbutanoic acid, (5) ethane-1,2-diol, (6) 2,3-butanediol monoacetate, (7) (S)-2-aminopentanoic acid, (8) 2-methyl-1,3-propanediol, (9) 2-methylmalonic acid, (10) propanoic acid, (11) acetic acid, (12) butanoic acid, (13) 1,3-butanediol, (14) methyl 3-hydroxypentanoate, (15) 3-hydroxy-2-methylbutanoic acid, (16) octanoic acid, (17) 4-oxopentanoic acid, and (18) 2-butenedioic acid. It was possible due to the

Fig. 7 Acidity of the nanocatalysts
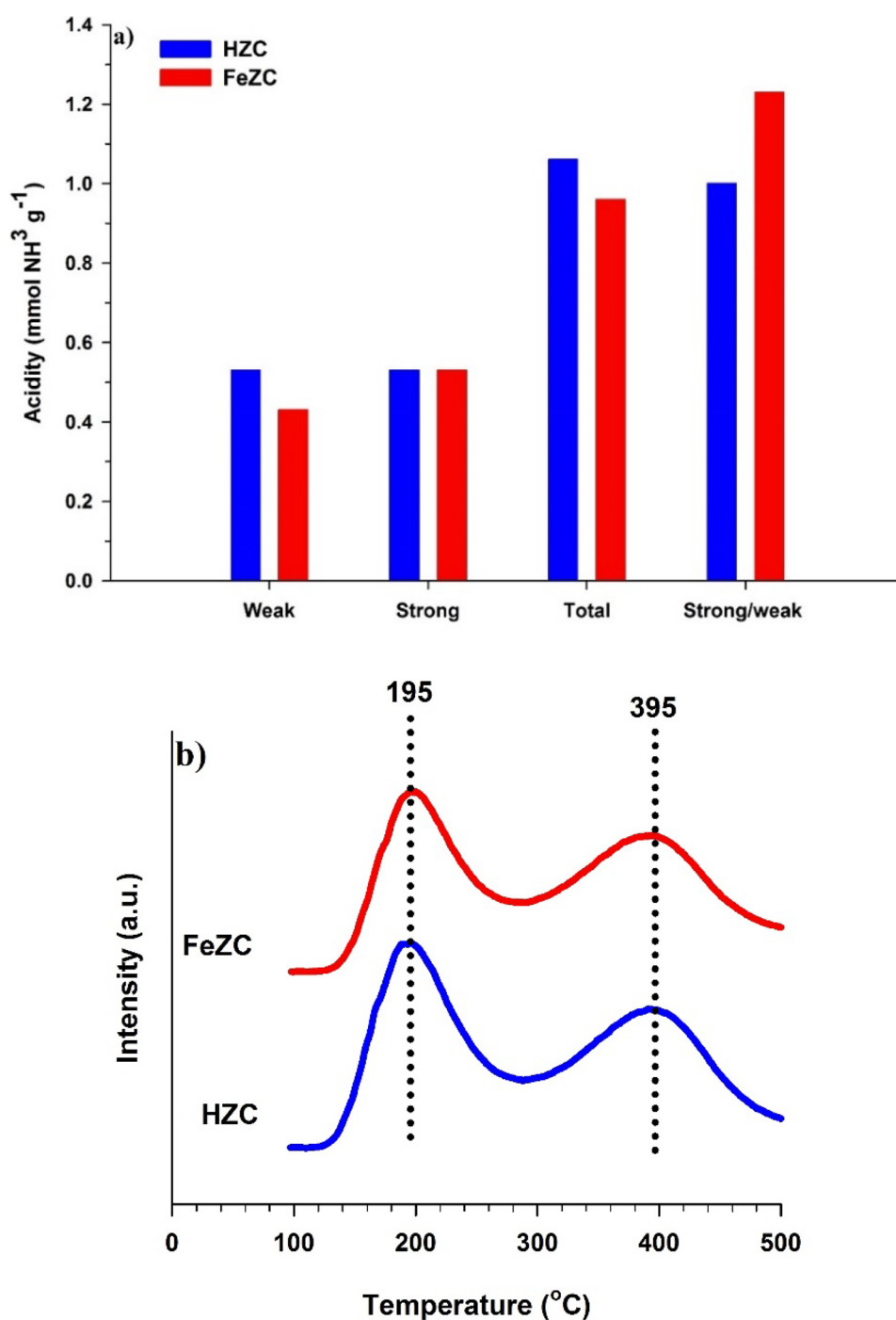
breaking of C–N and C–C bonds at NR in earlier stages, compounds with OH and COOH functional groups were formed. These intermediates can be altered to the short-chain carboxylic acids by further oxidation and finally to CO_2 and H_2O. It must be noted that, alongside the identified compounds, many other chromatographic peaks were also observed. But since their match factor of mass spectrums was very low, it was not possible to recognize them favorably.

Stability of the Electrodes

For examining the stability of the electrodes, repeated-batch operations were performed. According to Fig. 9, during ten repeated runs, the electrodes showed slight decrease of decolorization efficiency from the first run to the last one. The decolorization decrease amount was 4.46% (92.44–87.98%) after ten runs. Therefore, the results indicated that the electrodes had a good stability and
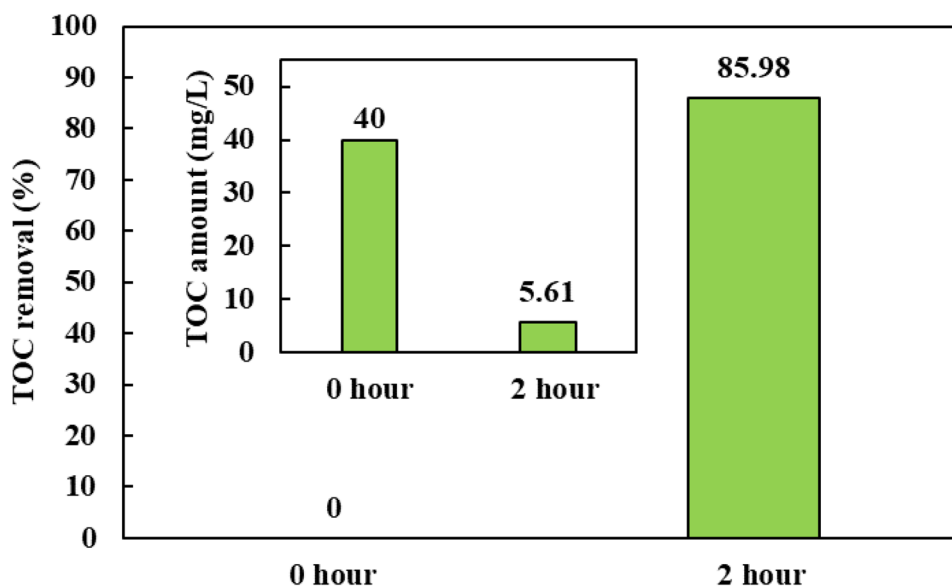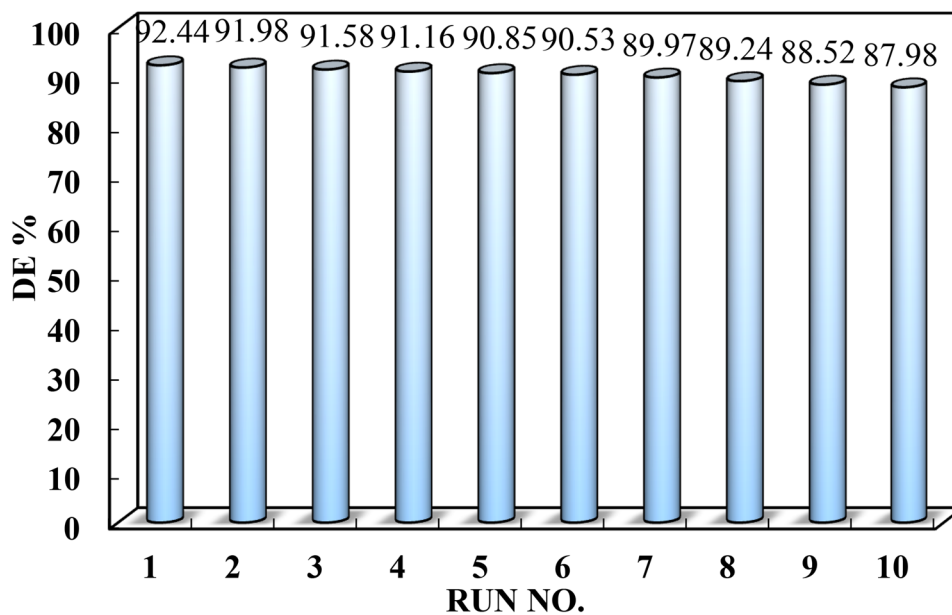
Fig. 8 TOC changes of NR solution over time

Fig. 9 DE (%) of graphite electrode during ten batch operations

possessed reasonable reusability in repetitive degradation operations.

Conclusions

In the present work, the EF process for the decolorization of NR from contaminated water was investigated via a couple of graphite electrodes. Thirty-one experiments were done via RSM. The results showed that in the applied current of 200 mA, the amount of Fe^{2+} 2%, the initial NR concentration of 40 mg/L and pH = 3 during 40 min of reaction time, the maximum decolorization efficiency value was 85.88% at homogenous EF,

90.32% and 92.44% at heterogeneous EF using HZC and FeZC nanocatalyst, respectively. The results of the experimental part were compared by predictions using Minitab 16 software. The correlation coefficient found between the experimental and the model results was 99.7%. FT-IR, XRD, BET, and TPD analyses were performed to confirm the successful synthesis of HZC and FeZC catalysts. UV–Vis, TOC, and GC-MS analysis were performed to analyze the successful degradation of the NR. The resulting compound was analyzed by GC-MS, and 18 compounds were successfully identified. The TOC results showed about 85.98% of NR mineralization efficiency. Due to the low cost and high decolorization efficiency of this method, it can be used for the removal of organic pollutants such as dyes.

References

1. R. Dewil, D. Mantzavinos, I. Poulios, M.A. Rodrigo, New perspectives for advanced oxidation processes. J. Environ. Manage. **195**, 93–99 (2017)

2. C.A. Martínez-Huitle, M.A. Rodrigo, I. Sirés, O. Scialdone, Single and coupled electrochemical processes and reactors for the abatement of organic water pollutants: a critical review. Chem. Rev. **115**(24), 13362–13407 (2015)

3. E. Lacasa, P. Cañizares, F.C. Walsh, M.A. Rodrigo, C. Ponce-de-Leon, Removal of methylene blue from aqueous solutions using an Fe^{2+} catalyst and in-situ H_2O_2 generated at gas diffusion cathodes. Electrochim. Acta **308**, 45–53 (2019)

4. J.I. Colades, C.P. Huang, J.D. Retumban, S. Garcia-Segura, M.D.G. de Luna, Electrochemically-driven dosing of iron (II) for autonomous electro-Fenton processes with in situ generation of H_2O_2. J. Electroanal. Chem. **856**, 113639 (2020)

5. K. Wu, F. Zhang, H. Wu, C. Wei, The mineralization of oxalic acid and bio-treated coking wastewater by catalytic ozonation using nickel oxide. Environ. Sci. Pollut. Res. **25**(3), 2389–2400 (2018)

6. F. Ali, J.A. Khan, N.S. Shah, M. Sayed, H.M. Khan, Carbamazepine degradation by UV and UV-assisted AOPs: kinetics, mechanism and toxicity investigations. Process Saf. Environ. Prot. **117**, 307–314 (2018)

7. M. Zheng, S. Wu, Q. Dong, X. Huang, Z. Yuan, Y. Liu, Achieving mainstream nitrogen removal via the nitrite pathway from real municipal wastewater using intermittent ultrasonic treatment. Ultrason. Sonochem. **51**, 406–411 (2019)

8. M. Behrouzeh, M. Abbasi, S. Osfouri, M.J. Dianat, Treatment of DMSO and DMAC wastewaters of various industries by employing Fenton process: process performance and kinetics study. J. Environ. Chem. Eng. **8**(1), 103597 (2020)

9. M. Ranjbar, N. Majidian, M. Samipourgiri, Heterogeneous electro-Fenton process by MWCNT-Ce/WO_3 nanocomposite modified GF cathode for catalytic degradation of BTEX: process optimization using response surface methodology. Electrocatalysis **10**(6), 628–642 (2019)

10. G. Ren, M. Zhou, P. Su, W. Yang, X. Lu, Y. Zhang, Simultaneous sulfadiazines degradation and disinfection from municipal secondary effluent by a flow-through electro-Fenton process with graphene-modified cathode. J. Hazard. Mater. **368**, 830–839 (2019)

11. F.C. Moreira, R.A. Boaventura, E. Brillas, V.J. Vilar, Electrochemical advanced oxidation processes: a review on their application to synthetic and real wastewaters. Appl. Catal. B: Environ. **202**, 217–261 (2017)

12. G. Divyapriya, I.M. Nambi, J. Senthilnathan, An innate quinone functionalized electrochemically exfoliated graphene/Fe_3O_4 composite electrode for the continuous generation of reactive oxygen species. Chem. Eng. J. **316**, 964–977 (2017)

13. A.M. Gholizadeh, M. Zarei, M. Ebratkhahan, A. Hasanzadeh, F. Vafaei, Removal of Phenazopyridine from wastewater by merging biological and electrochemical methods via Azolla filiculoides and electro-Fenton process. J. Environ. Manage. **254**, 109802 (2020)

14. Y. Zhang, A. Wang, S. Ren, Z. Wen, X. Tian, D. Li, J. Li, Effect of surface properties of activated carbon fiber cathode on mineralization of antibiotic cefalexin by electro-Fenton and photoelectro-Fenton treatments: mineralization, kinetics and oxidation products. Chemosphere **221**, 423–432 (2019)

15. S. Chen, L. Tang, H. Feng, Y. Zhou, G. Zeng, Y. Lu, J. Yu, X. Ren, B. Peng, X. Liu, Carbon felt cathodes for electro-Fenton process

16. N. Fernández-Sáez, D.E. Villela-Martinez, F. Carrasco-Marín, A.F. Pérez-Cadenas, L.M. Pastrana-Martínez, Heteroatom-doped graphene aerogels and carbon-magnetite catalysts for the heterogeneous electro-Fenton degradation of acetaminophen in aqueous solution. J. Catal. **378**, 68–79 (2019)

17. A. Hasanzadeh, A. Khataee, M. Zarei, S.W. Joo, Photo-assisted electrochemical abatement of trifluralin using a cathode containing a C60-carbon nanotubes composite. Chemosphere **199**, 510–523 (2018)

18. K.C. Nakamura, L.S. Guimarães, A.G. Magdalena, A.C.D. Angelo, A.R. De Andrade, S. Garcia-Segura, A.R. Pipi, Electrochemically-driven mineralization of Reactive Blue 4 cotton dye: on the role of in situ generated oxidants. J. Electroanal. Chem. **840**, 415–422 (2019)

19. M. Zarei, D. Salari, A. Niaei, A. Khataee, Peroxi-coagulation degradation of CI Basic Yellow 2 based on carbon-PTFE and carbon nanotube-PTFE electrodes as cathode. Electrochim. Acta **54**(26), 6651–6660 (2009)

20. M. Zarei, F.B. Nahand, A. Khataee, A. Hasanzadeh, Removal of nalidixic acid from aqueous solutions using a cathode containing three-dimensional graphene. J. of Water Process Eng. **32**, 100978 (2019)

21. F. Sopaj, N. Oturan, J. Pinson, F.I. Podvorica, M.A. Oturan, Effect of cathode material on electro-Fenton process efficiency for electrocatalytic mineralization of the antibiotic sulfamethazine. Chem. Eng. J. **384**, 123249 (2020)

22. Y.J. Choe, J. Kim, Y.B. Ji, S.H. Kim, An Electro-Fenton System with Magnetite Coated Stainless Steel Mesh as Cathode (Catal, Today, 2019).

23. Y.Y. Lou, F. Geneste, I. Soutrel, A. Amrane, F. Fourcade, Alachlor dechlorination prior to an electro-Fenton process: influence on the biodegradability of the treated solution. Sep. Purif. Technol. **232**, 115936 (2020)

24. M. Shoorangiz, M.R. Nikoo, M. Salari, G.R. Rakhshandehroo, M. Sadegh, Optimized electro-Fenton process with sacrificial stainless steel anode for degradation/mineralization of ciprofloxacin. Process Saf. Environ. Prot. **132**, 340–350 (2019)

25. X. Zhang, J. Fu, Y. Zhang, L. Lei, A nitrogen functionalized carbon nanotube cathode for highly efficient electrocatalytic generation of H_2O_2 in Electro-Fenton system. Sep. Purif. Technol. **64**(1), 116–123 (2008)

26. C. Bruguera-Casamada, R.M. Araujo, E. Brillas, I. Sirés, Advantages of electro-Fenton over electrocoagulation for disinfection of dairy wastewater. Chem. Eng. J. **376**, 119975 (2019)

27. M. Fayazi, M. Ghanei-Motlagh, Electrochemical mineralization of Methylene blue dye using electro-Fenton oxidation catalyzed by a novel Sepiolite/Pyrite nanocomposite. Inter. J. Environ. Sci. Technol. (2020)

28. M.T. Yagub, T.K. Sen, S. Afroze, H.M. Ang, Dye and its removal from aqueous solution by adsorption: a review. Adv. Colloid Interface Sci. **209**, 172–184 (2014)

29. J. Yu, X. Wang, P.L. Yue, Optimal decolorization and kinetic modeling of synthetic dyes by Pseudomonas strains. Water Res. **35**(15), 3579–3586 (2001)

30. Z. He, S. Song, H. Zhou, H. Ying, J. Chen, CI Reactive Black 5 decolorization by combined sonolysis and ozonation. Ultrason. Sonochem. **14**(3), 298–304 (2007)

31. S. Figueroa, L. Vazquez, A. Alvarez-Gallegos, Decolorizing Stextile wastewater with Fenton's reagent electrogenerated with a solar photovoltaic cell. Water Res. **43**(2), 283–294 (2009)

32. M. Iram, C. Guo, Y. Guan, A. Ishfaq, H. Liu, Adsorption and magnetic removal of neutral red dye from aqueous solution using Fe_3O_4 hollow nanospheres. J. Hazard. Mater. **181**(1–3), 1039–1050 (2010)

33. M. Rostamizadeh, A. Jafarizad, S. Gharibian, High efficient decolorization of Reactive Red 120 azo dye over reusable Fe-ZSM-5 nanocatalyst in electro-Fenton reaction. Sep. Purif. Technol. **192**, 340–347 (2018)

34. A.R. Khataee, M. Zarei, L. Moradkhannejhad, Application of response surface methodology for optimization of azo dye removal by oxalate catalyzed photoelectro-Fenton process using carbon nanotube-PTFE cathode. Desalination **258**(1–3), 112–119 (2010)

35. M.E. Olya, M.B. Kasiri, H. Aleboyeh, A. Aleboyeh, Application of response surface methodology to optimise CI Acid Orange 7 azo dye mineralization by UV/H_2O_2 process. J. Adv. Oxid. Technol. **11**(3), 561–567 (2008)

36. D.M. Wardrop, R.H. Myers, Some response surface designs for finding optimal conditions. J. stat. plan. infer. **25**(1), 7–28 (1990)

37. P. Nidheesh, R. Gandhimathi, Trends in electro-Fenton process for water and wastewater treatment: an overview. Desalination **299**, 1–15 (2012)

38. J.P. Kushwaha, V.C. Srivastava, I.D. Mall, Organics removal from dairy wastewater by electrochemical treatment and residue disposal. Sep. Purif. Technol. **76**(2), 198–205 (2010)

39. M. Umar, H.A. Aziz, M.S. Yusoff, Trends in the use of Fenton, electro-Fenton and photo-Fenton for the treatment of landfill leachate. Waste Manage. (Oxford) **30**(11), 2113–2121 (2010)

40. A.A. Aziz, W.M.A.W. Daud, Oxidative mineralisation of petroleum refinery effluent using Fenton-like process. Chem. Eng. Res. Des. **90**(2), 298–307 (2012)

41. M. Zarei, A. Khataee, R. Ordikhani-Seyedlar, M. Fathinia, Photoelectro-Fenton combined with photocatalytic process for degradation of an azo dye using supported TiO_2 nanoparticles and carbon nanotube cathode: neural network modeling. Electrochim. Acta **55**(24), 7259–7265 (2010)

42. M. Rostamizadeh, F. Yaripour, Dealumination of high silica H-ZSM-5 as long-lived nanocatalyst for methanol to olefin conversion. J. Taiwan Inst. Chem. Eng. **71**, 454–463 (2017)

43. S.M. Campbell, X.-Z. Jiang, R.F. Howe, Methanol to hydrocarbons: spectroscopic studies and the significance of extra-framework aluminium. Micropor. Mesopor. Mat. **29**(1–2), 91–108 (1999)

44. M. Rostamizadeh, A. Taeb. Synthesis and characterization of HZSM-5 catalyst for methanol to propylene (MTP) reaction. Synth. React. Inorg, M. **46**(5), 665–671 (2016)

45. E. Rebrov, G. Seijger, H. Calis, M. de Croon, C. van Den Bleek, J. Schouten, The preparation of highly ordered single layer ZSM-5 coating on prefabricated stainless steel microchannels. Appl. Catal. A: Gen. **206**(1), 125–143 (2001)

46. M.J.D. Mahboub, A. Ahmadpour, H. Rashidi, Improving methane storage on wet activated carbons at various amounts of water. J. Fuel Chem. Technol. **40**(4), 385–389 (2012)

47. M.J.D. Mahboub, M. Rostamizadeh, J.-L. Dubois, G.S. Patience, Partial oxidation of 2-methyl-1, 3-propanediol to methacrylic acid: experimental and neural network modeling. RSC advances **6**(115), 114123–114134 (2016)

48. Y. Sun, H. Yan, D. Liu, D. Zhao, A comparative study on the dehydration of monoethanolamine over cesium phosphate modified zeolite catalysts. Catal. Commun. **9**(5), 924–930 (2008)

49. L.M. Kustov, V. Kazansky, P. Ratnasamy, Spectroscopic investigation of iron ions in a novel ferrisilicate pentasil zeolite. Zeolites **7**(1), 79–83 (1987)